Check for updates

Dynamic shapes of floppy vesicles enclosing active Brownian particles with membrane adhesion†

Priyanka Iyer, [ID] Gerhard Gompper [ID] and Dmitry A. Fedosov [ID] *

Recent advances in micro- and nano-technologies allow the construction of complex active systems from biological and synthetic materials. An interesting example is active vesicles, which consist of a membrane enclosing self-propelled particles, and exhibit several features resembling biological cells. We investigate numerically the behavior of active vesicles, where the enclosed self-propelled particles can adhere to the membrane. A vesicle is represented by a dynamically triangulated membrane, while the adhesive active particles are modelled as active Brownian particles (ABPs) that interact with the membrane *via* the Lennard-Jones potential. Phase diagrams of dynamic vesicle shapes as a function of ABP activity and particle volume fraction inside the vesicle are constructed for different strengths of adhesive interactions. At low ABP activity, adhesive interactions dominate over the propulsion forces, such that the vesicle attains near static configurations, with protrusions of membrane-wrapped ABPs having ring-like and sheet-like structures. At moderate particle densities and strong enough activities, active vesicles show dynamic highly-branched tethers filled with string-like arrangements of ABPs, which do not occur in the absence of particle adhesion to the membrane. At large volume fractions of ABPs, vesicles fluctuate for moderate particle activities, and elongate and finally split into two vesicles for large ABP propulsion strengths. We also analyze membrane tension, active fluctuations, and ABP characteristics (*e.g.*, mobility, clustering), and compare them to the case of active vesicles with non-adhesive ABPs. The adhesion of ABPs to the membrane significantly alters the behavior of active vesicles, and provides an additional parameter for controlling their behavior.

1. Introduction

In recent years, there has been a growing interest in a variety of active matter systems which operate far from equilibrium and show rich dynamical behaviors and functions.[1–4] Examples include biological systems ranging from cells to tissues,[5,6] collections of micro-swimmers,[7,8] and active engineered systems.[9,10] The growing research interest has been nurtured by rapid developments in microscale and nanoscale technologies which already allow for a well-controlled construction of complex multicomponent active systems and materials.[9,11,12] A prominent example is cell-mimicking systems, which are generally constructed from cell-based biological constituents, and include active nematics made of driven biofilaments,[13,14] and growing and dividing droplet-based or vesicle-based

Theoretical Physics of Living Matter, Institute of Biological Information Processing and Institute for Advanced Simulation, Forschungszentrum Jülich, 52425 Jülich, Germany. E-mail: p.iyer@fz-juelich.de, g.gompper@fz-juelich.de, d.fedosov@fz-juelich.de

† Electronic supplementary information (ESI) available: Four movies, illustrating different shape changes of active vesicles, whose description is provided in Appendix E. See DOI: https://doi.org/10.1039/d3sm00004d

compartments.[15,16] In many other examples, biological materials are combined with active synthetic constituents with a hope to mimic various biological systems or even go beyond their functionality.[17,18] Here, an interesting example is a closed membrane enclosing biological micro-swimmers such as bacteria[19–21] or synthetic self-propelled particles.[18,22–25] Active components inside the soft confinement exert forces on the surface, leading to highly dynamic non-equilibrium shape changes which resemble certain processes in living cells such as the formation of filopodia and lamellipodia,[5,26,27] and active shape fluctuations of the membrane.[28–30]

The main features that differentiate active vesicles from various membrane structures in equilibrium[31,32] are active force generation due to the enclosed active components and dynamic shape changes of the membrane. For instance, swimming bacteria or motile synthetic particles within a vesicle induce the formation of tethers and protrusions which dynamically elongate and retract.[18–20] In equilibrium, string-of-pearls-like and tubular protrusions can be formed by amphipathic peptides or BAR domain proteins,[32,33] but these structures are static and correspond to a minimum of total energy. Therefore, different

physical mechanisms govern the formation of various membrane structures in equilibrium and in non-equilibrium active vesicles. In particular, the curvature-induced clustering of active particles[34–36] at the membrane leads to the concentration of active forces at spots with a high curvature. Moreover, there exists a positive feedback mechanism between the induction of strong curvature by active particles and their clustering in places with large curvature, so that the shape of active vesicles is altered dynamically and collectively.[18,23] Furthermore, active components within a vesicle give rise to a significant increase in membrane tension due to the swim pressure exerted by the particles.[37]

Apart from active forces, the deformation of a membrane can also occur as a consequence of adhesive interactions between the membrane and enclosed particles.[38–42] In particular, adhesive interactions result in partial or full wrapping of the particles by the membrane, which can significantly reduce the force required for tether formation. Furthermore, the adhesion of multiple particles to the membrane often induces membrane-mediated interactions between the particles, leading to a cooperative wrapping of particles by the membrane[41] and the formation of various particle structures at the membrane surface.[43–47] These interactions can enhance or reduce the clustering of active particles, potentially altering the behavior of active vesicles. In addition, it is plausible to expect that the adhesive interactions between the particles and the membrane can facilitate the existence of active forces away from the membrane (i.e., pulling forces), which is not possible for non-adhesive active particles which exert pushing forces toward the membrane. Finally, adhesive interactions of particles and pathogens with a cell membrane are essential for a variety of biological processes such as membrane translocation, viral budding, and phagocytosis.[48–51]

In our study, we investigate numerically the combined effect of particle activity and adhesive interactions on the behavior of active vesicles. Fluid membrane vesicles are modeled as dynamically triangulated surfaces[52,53] enclosing a number of active Brownian particles (ABPs). Adhesive interactions between the ABPs and the membrane are incorporated through the Lenard-Jones potential, whose strength is varied to induce various degrees of ABP wrapping by the membrane. A phase diagram of dynamic vesicle shapes is constructed as a function of the ABP propulsion strength and the volume fraction of particles within the vesicle. The presence of ABP adhesion to the membrane leads to qualitative changes in the phase diagram in comparison to that for non-adhesive ABPs.[18] For a weak particle activity, the adhesion interactions dominate, yielding nearly static vesicle shapes, which are similar to those in equilibrium with only adhesive interactions present. For moderate particle activities and volume fractions, complex tether structures filled with string-like arrangements of ABPs are formed, and characterized by a number of branching points. In contrast, for non-adhesive ABPs, the formed tethers show no significant branching, and the ABPs generally cluster at the end of membrane tethers.[18,23] Finally, for a strong particle propulsion, active forces from the ABPs dominate over the adhesion interaction, and the resulting behavior of active

vesicles is similar to those with non-adhesive ABPs. Also, membrane properties of the active vesicles and the characteristics of ABP clustering and mobility are analysed and compared to those of non-adhesive ABPs.

The article is organized as follows. Section 2 provides all necessary details about the employed methods and models, including the parameters used in simulations. Section 3.1 presents dynamic shape diagrams for two strengths of the ABP adhesion to the membrane. Membrane tension and the importance of ABP adhesion are discussed in Section 3.2. Vesicle shape fluctuations are analysed in Section 3.3, and ABP characteristics are presented in Section 3.4. Finally, we conclude in Section 4.

2. Methods and models

An active vesicle is represented by a closed fluid membrane of spherical topology with radius R, enclosing N_p active Brownian particles (ABPs). The activity of the particles is described by the dimensionless Peclet number $Pe = \sigma v_p / D_t$, where σ is the particle diameter, v_p is the propulsion velocity, and D_t is the translational diffusion coefficient. Note that Pe is a measure of the propulsion force f_p of ABPs, with $v_p = f_p / \gamma_p$ and $D_t = k_B T / \gamma_p$, where γ_p is the translational friction coefficient, so that $Pe = f_p \sigma / k_B T$. Particle volume fraction within the vesicle is given by $\phi = N_p (\sigma / 2R)^3$. Table 1 presents all simulation parameters.

2.1 Model of adhesive active Brownian particles

ABPs are modeled as active spherical particles without hydrodynamic interactions. Each ABP experiences a propulsion force f_p that acts along an orientation vector $\mathbf{e}_i$. The force results in a propulsion velocity $v_p = f_p / \gamma_p$. The orientation vector $\mathbf{e}_i$ is subject to orientational diffusion $\dot{\mathbf{e}}_i = \boldsymbol{\zeta}_i \times \mathbf{e}_i$, where $\boldsymbol{\zeta}_i$ is a Gaussian random process with $\langle \boldsymbol{\zeta}_i(t) \rangle = 0$ and $\langle \boldsymbol{\zeta}_i(t) \cdot \boldsymbol{\zeta}_j(t') \rangle = 6 D_r \delta_{ij} \delta(t - t')$ with a rotational diffusional coefficient D_r. D_r is related to the ABP diameter σ and translational diffusion coefficient D_t as $D_t = D_r \sigma^2 / 3$.

Interactions between different ABPs and membrane particles are implemented through the 12-6 Lennard-Jones (LJ) potential

$$U(r) = 4\varepsilon \left[\left(\frac{\sigma_{LJ}}{r} \right)^{12} - \left(\frac{\sigma_{LJ}}{r} \right)^{6} \right], \qquad (1)$$

where ε is the potential strength, and σ_{LJ} is the characteristic excluded-volume distance. For ABP-ABP interactions, $\sigma_{LJ} = \sigma$, and the potential cutoff is set to $r_c^{p-p} = 2^{1/6}\sigma$, imposing purely repulsive interactions. For attractive ABP-membrane interactions, $\sigma_{LJ} = \sigma/2$ (i.e. the ABP radius), and the potential cutoff is set to $r_c^{p-m} = 2^{1/6}\sigma$, so that only a single layer of ABPs is attracted to the membrane. Note that the membrane particles are considered to be point-like, such that the modeled membrane is a surface with nearly zero thickness. Therefore, the only relevant length scale for ABP-membrane interactions is the particle diameter σ (see Appendix A for more details).

Table 1 Parameters used for simulations of vesicles enclosing adhesive ABPs both in model and physical units. The principal properties represent basic scaling units, which can be selected. However, all other dependent parameters and results are presented in units of R, k_BT, and τ. The principle properties in physical units correspond to the experimental setup in ref. 18. $N_t = 2N_v - 4$ is the number of triangular faces in the vesicle discretization

Parameters	Model units	Physical units
Principal properties		
Vesicle radius in equilibrium R	32	8 μm
Thermal energy unit k_BT	0.2	4.14×10^{-21} J
Time scale $\tau = \gamma_p R^2/\kappa_c$	1.28×10^5	7.3 s
Investigated properties		
Peclet number Pe $= \sigma v_p/D_t$	0–400	0–400
Total number of ABPs N_p	30–1458	30–1458
ABP volume fraction $\phi = N_p(\sigma/2R)^3$	9×10^{-3}–3.56×10^{-1}	9×10^{-3}–3.56×10^{-1}
ABP diameter σ	$R/8$	1 μm
Vesicle properties		
Number of vertices N_v	30 000	30 000
Bending rigidity κ_c	$20k_BT$	8.28×10^{-20} J
Average bond length l_b	$4R\sqrt{\dfrac{\pi}{N_t\sqrt{3}}}$	0.176 μm
Bond stiffness k_b	$80k_BT$	3.31×10^{-19} J
Minimum bond length l_{min}	$0.6l_b$	0.11 μm
Potential cutoff length l_{c1}	$0.8l_b$	0.14 μm
Potential cutoff length l_{c0}	$1.2l_b$	0.21 μm
maximum bond length l_{max}	$1.4l_b$	0.25 μm
Desired vesicle area A_0	$4\pi R^2$	8.04×10^2 μm^2
local area stiffness k_a	$6.43 \times 10^6 k_BT/A$	3.3×10^{-5} J m^{-2}
Friction coefficient γ_m	$0.4k_BT\tau/R2$	1.9×10^{-10} J s m^{-2}
Flipping frequency ν	$6.4 \times 10^6\tau^{-1}$	8.8×10^5 s^{-1}
Flipping probability p_f	0.3	0.3
ABP properties		
Translational friction γ_p	$20k_BT\tau/R^2$	9.4×10^{-9} J s m^{-2}
Translational diffusion D_t	k_BT/γ_p	4.4×10^{-13} m^2 s^{-1}
Rotational diffusion D_r	$3D_t/\sigma^2$	1.32 s^{-1}
LJ potential depth (adhesion energy) ε	2.5–3.5k_BT	1.03×10^{-20}–1.45×10^{-20} J

2.2 Membrane model

The vesicle is modeled by a dynamically triangulated membrane of spherical topology consisting of N_v linked vertices.[52,53] The interaction between linked vertices is controlled *via* a tethering potential[52,54] that is a combination of attractive and repulsive parts

$$U_{att}(r) = \begin{cases} k_b \dfrac{\exp[1/(l_{c_0} - r)]}{l_{max} - r}, & \text{if } r > l_{c_0}, \\ 0, & \text{if } r \le l_{c_0}, \end{cases} \quad (2)$$

$$U_{rep}(r) = \begin{cases} k_b \dfrac{\exp[1/(r - l_{c_1})]}{r - l_{min}}, & \text{if } r < l_{c_1}, \\ 0, & \text{if } r \ge l_{c_1}. \end{cases} \quad (3)$$

Here, k_b is the bond stiffness, l_{min} and l_{max} are the minimum and maximum bond lengths, and l_{c_0} and l_{c_1} are the potential cutoff lengths.

The membrane bending elasticity is modeled by the Helfrich curvature energy,[55]

$$U_{bend} = 2\kappa_c \oint \bar{c}^2 \, \mathrm{d}A, \quad (4)$$

where κ_c is the bending rigidity and $\bar{c} = (c_1 + c_2)/2$ is the mean local curvature at the membrane surface element dA. In the discretized form, it becomes[56,57]

$$U_{bend} = 2\kappa_c \sum_{i=1}^{N_v} \sigma_i \bar{c}_i^2, \quad (5)$$

where $\bar{c}_i = \mathbf{n}_i \cdot \sum_{j(i)} \sigma_{ij}\mathbf{r}_{ij}/(2\sigma_i r_{ij})$ is the discretized mean curvature at vertex i, $\mathbf{n}_i$ is the unit normal at the membrane vertex i, $\sigma_i = \sum_{j(i)} \sigma_{ij} r_{ij}$ is the area corresponding to vertex i (the area of the dual cell), $j(i)$ corresponds to all vertices linked to vertex i, and $\sigma_{ij} = r_{ij}(\cot\theta_1 + \cot\theta_2)/2$ is the length of the bond in the dual lattice, where θ_1 and θ_2 are the angles at the two vertices opposite to the edge ij in the dihedral. In practice, since the dihedral terms corresponding to σ_{ij} are additive, the local curvature at each vertex can be calculated by summing over contributions from all triangles containing that vertex.

The area conservation is imposed locally to each triangle by the potential

$$U_A = \frac{k_a}{2} \sum_{i=1}^{N_t} \frac{(A_i - A_l)^2}{A_l}, \quad (6)$$

where $N_t = 2(N_v - 2)$ is the number of triangles, $A_l = A_0/N_t$ is the targeted local area (A_0 is the total membrane area), A_i is the instantaneous local area, and k_a is the local-area conservation

coefficient. We do not impose any volume constraints, and therefore, the vesicle volume is free to change within physical bounds of a nearly inextensible membrane. Therefore, our simulations represent a case of floppy vesicles.

Membrane fluidity is modelled by a stochastic flipping of bonds following a Monte–Carlo scheme. The bond shared by each pair of adjacent triangles can be flipped to connect the two previously unconnected vertices.[52,57] The flipping is performed with a frequency ν and probability p_f. An energetically favorable bond flip is accepted with a probability of $p = 1$. For an energetically unfavorable flip, the resulting change in energy due to an attempted bond flip $\Delta U = \Delta U_{att} + \Delta U_{rep} + \Delta U_A$ determines the probability of the flipping as $p = \exp[-\Delta U/k_B T]$. The resulting membrane fluidity can be characterized by a 2D membrane viscosity for the selected frequency ν and flipping probability p_f.[54,58] Note that the two bond-flipping parameters ν and p_f can conceptually be combined into a single flipping probability or frequency. However, the use of two parameters is computationally advantageous, as the flipping procedure is computationally expensive. With two parameters, the flipping can be performed not every time step, which is controlled by ν, while an implementation with a single parameter would require checks for bond flipping at every time step.

2.3 Equation of motion

The system evolves in time according to the Langevin equation

$$m\ddot{\mathbf{r}}_i = -\nabla_i U_{tot} - \gamma \dot{\mathbf{r}}_i + \sqrt{2\gamma k_B T}\,\boldsymbol{\xi}_i(t), \qquad (7)$$

where m is the mass of membrane particle or ABP, $\ddot{\mathbf{r}}_i$ and $\dot{\mathbf{r}}_i$ represent the second and first time derivatives of particle positions, ∇_i is the spatial derivative at particle i, and U_{tot} is the sum of all interaction potentials described above. The effect of a viscous fluid is mimicked by the friction co-efficient γ, whose value can be different for membrane particles and ABPs, see Table 1. Thermal fluctuations are modelled as a Gaussian random process $\boldsymbol{\xi}_i$ with $\langle \boldsymbol{\xi}_i(t) \rangle = 0$ and $\langle \boldsymbol{\xi}_i(t) \cdot \boldsymbol{\xi}_j(t') \rangle = 6\delta_{ij}\delta(t - t')$. Inertial effects are minimized by performing the simulations in the over-damped limit with m and γ such that $\tau_t = m/\gamma < 1 \ll \tau_r = D_r^{-1} \approx 0.1\tau$. The positions and velocities of all particles are integrated using the velocity-Verlet algorithm.[59]

2.4 ABP adhesion and membrane wrapping

Adhesion interactions between the ABPs and the membrane are mediated by the LJ potential whose strength is characterized by the potential depth ε. Adhesion strength determines the degree of particle wrapping by the membrane, with energetic costs due to membrane bending and tension. The ratio of the membrane bending modulus κ and the lateral tension λ defines a length $\tilde{l} = \sqrt{\kappa/\lambda}$, below which membrane deformations are mainly controlled by the bending energy, while deformations on length scales larger than $\tilde{l}$ are dominated by tension.[39] If tension is neglected and the membrane covers area $A_{wrap} \leq \pi\sigma^2$ of the particle (e.g., partial wrapping), the adhesion (E_{ad}) and bending (E_{bend}) energies are given by

$$E_{ad} = -\omega A_{wrap}, \quad E_{bend} = 8\kappa A_{wrap}/\sigma^2, \qquad (8)$$

where ω is the adhesion strength per unit area. In this case, the minimum of the total energy corresponds to complete wrapping of the particle by the membrane (i.e., $A_{wrap} = \pi\sigma^2$), which occurs for $\omega > \omega_{min} = 8\kappa/\sigma^2$.[38] Therefore, in the absence of membrane tension, the particle is in an unwrapped state for $\omega < \omega_{min}$, while the particle is fully wrapped for $\omega > \omega_{min}$ with no energy barrier to overcome. However, in the presence of tension, particle adhesion shows a continuous transition from the unwrapped to partially wrapped state at ω_{min}, while the transition to the fully wrapped state is discontinuous and has an energy barrier.[39]

To relate the adhesion strength ω per unit area and the strength ε of the LJ potential in simulations, we consider the attraction of a single membrane vertex to an ABP, such that $\varepsilon = 2\omega A_1$ with $2A_1$ being the area of the vertex. For the parameters in Table 1, the transition from the unwrapped to a wrapped state is expected at $\omega_{min} = 8\kappa/\sigma^2$ which implies $\varepsilon_c \simeq 4k_B T$. In our simulations, adhesive interactions between ABPs and the membrane are exerted up to a distance of σ from the membrane surface, and are therefore long ranged. Theoretical predictions of particle wrapping for long-ranged adhesive interactions indicate that the transition to the fully wrapped state is gradual,[41] which is consistent with the area A_{wrap} of particle wrapping as a function of ε shown in Fig. 1(a). A_{wrap} in simulations is calculated as the number of membrane vertices within a cutoff distance r_{adh} from the ABP center, multiplied by the vertex area $A_v = A_0/N_v$. Thus, the fully wrapped state requires adhesion interactions with $\varepsilon > \varepsilon_c$. For further simulations, we have selected two adhesion strengths of $\varepsilon = 2.5k_B T$ and $\varepsilon = 3.5k_B T$, which correspond to a moderate degree of wrapping illustrated in Fig. 1(b and c).

3. Results

3.1 Dynamic phase diagram

Fig. 2 presents phase diagrams of dynamic shape changes of active vesicles as a function of Pe and ϕ for two different adhesion strengths ε (see also Movies S1–S4, ESI†). At small Pe $\lesssim 50$, the formation of buds for low particle densities, ring-like aggregates of ABPs for intermediate ϕ values, and ABP aggregates with a hexagonal closed-packed (HCP) structure for large ϕ are observed and illustrated in Fig. 3 for Pe = 15. Some of these structures have previously been observed in studies of passive particles adhering to a membrane.[43–46] Furthermore, for Pe $\lesssim 50$, ABPs adhered to the membrane show little dynamics, suggesting that adhesive forces dominate over particle activity. As a result, active vesicles for Pe $\lesssim 50$ are close to an equilibrium state, with ABP aggregate structures similar to those of equilibrium systems at Pe = 0.

In the near-equilibrium "cauliflower" regime at low ABP densities, both individually wrapped particles and short strings of several ABPs within membrane tubes (see Fig. 3(a)) are observed due to the competition between repulsive curvature-mediated interactions[47] and the in-plane motion from ABP propulsion. As the ABP volume fraction is increased, strong
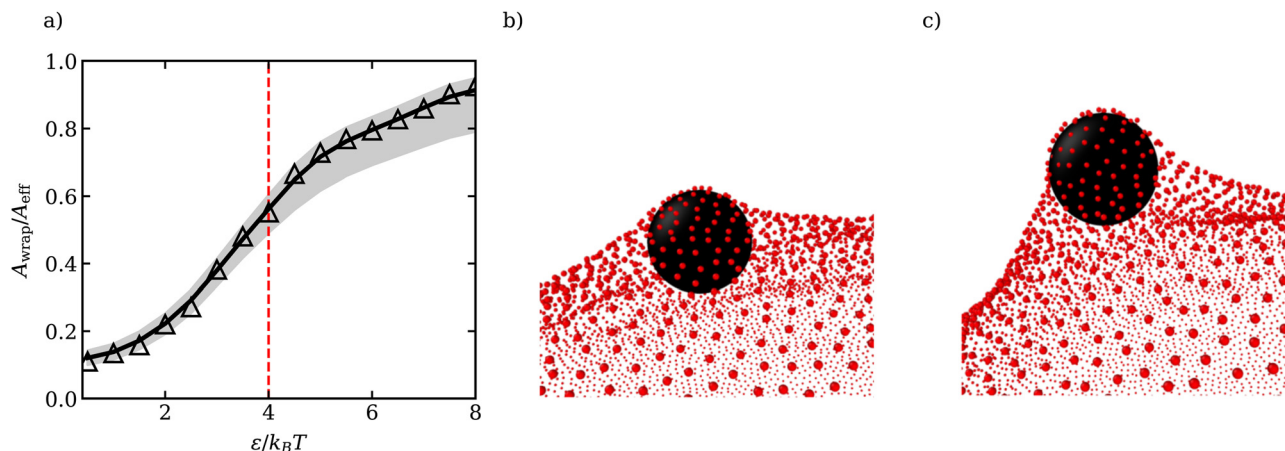
Fig. 1 (a) Fraction of wrapped area A_{wrap} of the ABP as a function of ε. A_{wrap} represents the area of membrane vertices around the cutoff distance $r_{\mathrm{adh}} = 1.16\sigma/2$ from the ABP (see Appendix A for the estimation of r_{adh}). The grey region corresponds to A_{wrap} estimates based on the cutoffs $r_{\mathrm{adh}} + \mu$ (lower bound) and $r_{\mathrm{adh}} + 3\mu$ (upper bound), where μ is the variance of the ABP-membrane distance distribution in the fully wrapped state (see Appendix A). The dashed red line marks theoretical predictions of the critical ε_{c} for the transition from unwrapped to fully wrapped state[38] and $A_{\mathrm{eff}} = 4\pi r_{\mathrm{adh}}^2$ is the effective particle area. Due to the long range of interactions between the particle and the membrane, the transition is gradual and the particle is only partially wrapped at ε_{c}.[41] (b and c) Partially wrapped states of a particle (black) by the membrane (red) for (b) $\varepsilon = 2.5k_{\mathrm{B}}T$ and (c) $\varepsilon = 3.5k_{\mathrm{B}}T$.
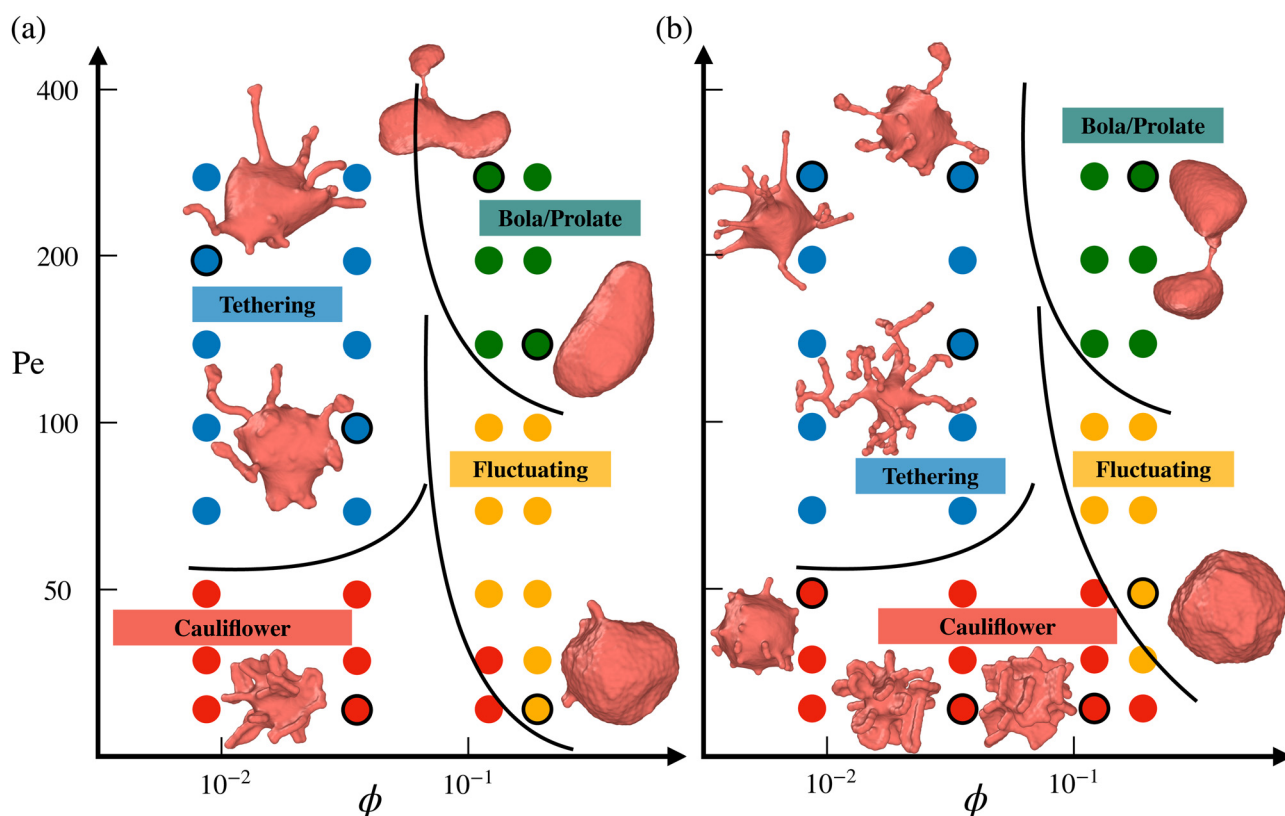

Fig. 2 Phase diagrams of vesicle-shape changes as a function of Pe and ϕ for two different adhesion strengths (a) $\varepsilon = 2.5k_{\mathrm{B}}T$ and (b) $\varepsilon = 3.5k_{\mathrm{B}}T$. Four regions are observed, including the tethering (blue symbols), bola/prolate (green symbols), fluctuating (yellow symbols), and cauliflower (red symbols) regimes. The points corresponding to the displayed snapshots have black outlines. The black lines provide an approximate demarcation of the different regimes, serving as a guide to the eye. For a visual illustration of dynamic shape changes of active vesicles, see also Movies S1–S4 (ESI†).

cooperative wrapping of ABPs is observed, as shown in Fig. 3(b and c). Here, it is likely that the gain in energy due to the cooperative wrapping overcomes the curvature-mediated repulsion.

Cooperative wrapping of several particles is also enhanced by the interaction range of an adhesion potential.[41] Furthermore, the vesicle is free to change its volume in our simulations, and
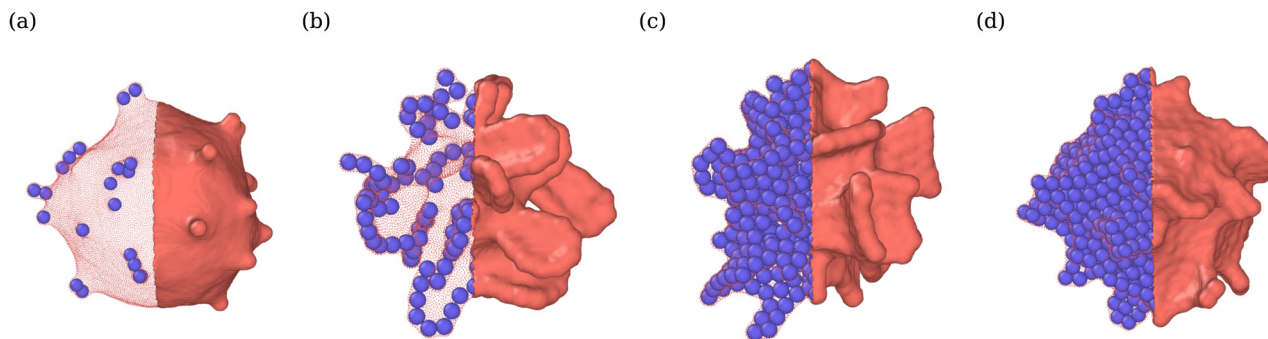
Fig. 3 Vesicle shapes in the near-equilibrium "cauliflower" regime at Pe = 15 and $\varepsilon = 3.5k_BT$ for (a) $\phi = 0.009$, (b) $\phi = 0.04$ (see Movie S4, ESI†), (c) $\phi = 0.12$, and (d) $\phi = 0.18$. Different nearly-frozen structures of the ABPs are observed, including ring-like and sheet-like arrangements. The left half of the membrane is made transparent so that the arrangement of ABPs is visible.

therefore, the area fraction of adhered membrane can be large. As a result, extreme deformations of the vesicle with protruding ring-like and sheet-like structures are observed and illustrated in Fig. 3(b and c). For the largest volume fraction of ABPs ($\phi = 0.18$), membrane deformations are reduced (see Fig. 3(d)) in comparison to the cases of $\phi = 0.04$ and $\phi = 0.12$, because the gain in adhered membrane area is restricted at some point by the volume of the ABP content. Therefore, if the vesicle volume were constrained to near-spherical values, membrane deformations are expected to be reduced, since the gain in adhered membrane would be restricted by an increase in membrane tension due to the constrained vesicle volume. Note that for the lower adhesion strength of $\varepsilon = 2.5k_BT$, membrane deformations are less pronounced than in the case of $\varepsilon = 3.5k_BT$ (see Fig. 2 for Pe $\lesssim 50$) due to the competition between adhesion and bending energies.

As Pe is increased, ABP propulsion starts to dominate over the adhesive forces, and the non-equilibrium nature of active vesicles becomes apparent. At low particle densities ($\phi \lesssim 0.07$), ABP activity leads to the formation of dynamic tether-like structures, which are filled by string-like arrangements of ABPs. This behavior is qualitatively different from the tether formation by ABPs in the absence of adhesive interactions, where particle clustering takes place at the end of a tether.[18,23] Note that the string-like arrangement of particles in membrane tubes is favored by long-ranged adhesive interactions.[41,60] Another qualitative difference of the formed tethered structures by adhesive ABPs in comparison to those by non-adhesive active particles[18,23] is that the tethered structures in Fig. 2 are often highly branched. Since ABPs spend a considerable time in string-like configurations within membrane tethers, ABPs can change their orientation due to rotational diffusion and initiate branch formation from the existing tether. In the absence of adhesive interactions, ABPs quickly travel between the base of a tether and its end (or vise versa), and thus cannot easily initiate branched tethers.[18,23] Therefore, adhesive interactions promote the formation of branched tether structures and stabilize them. At the lower adhesion strength of $\varepsilon = 2.5k_BT$, ABPs cluster more at tether ends than for the case of $\varepsilon = 3.5k_BT$, and result in less branched structures, as shown in Fig. 2. A similar effect is observed with increasing particle activity (or Pe), suggesting that branched tether structures and string-like arrangements of ABPs are indeed a consequence of particle adhesion to the membrane, which is lost when ABPs have a sufficient force to detach from the membrane. Note that the tethering regime for adhesive ABPs occurs at significantly lower Pe numbers when compared to the non-adhesive ABP case[18,23] because particle adhesion facilitates wrapping, reducing the energy barrier required for the formation of tethers.

At large particle densities ($\phi \gtrsim 0.07$) and for Pe values beyond the cauliflower regime, a fluctuating phase first develops, where shape changes of the vesicle are moderate and resemble membrane fluctuations. In Section 3.3, we will show that vesicle shape fluctuations for adhesive ABPs are different from those for the non-adhesive ABP case.[18] As Pe is further increased for $\phi \gtrsim 0.07$, the ABPs form large clusters which can push in opposing directions and result in vesicle elongation or even splitting into two vesicles, similar to the non-adhesive ABP case.[18] Thus, the effect of adhesive interactions is prevalent only for low to intermediate Pe values, where the adhesive forces are larger than or comparable to ABP propulsion forces.

The diagrams in Fig. 2 are primarily constructed through visual inspection of vesicle shapes and their dynamic changes. This is sufficient because the vesicle conformations in Fig. 2 display significant qualitative differences between the various phases: long thin tethers emerging from the mother vesicle in the tethering phase, nearly spherical shapes with strong fluctuations in the fluctuating phase, large asphericity and whole shape deformation in the bola/prolate phase, and nearly static vesicle shapes with several particle-filled protrusions in the cauliflower phase. Classification of vesicle shapes can also be based on a quantitative analysis of their characteristics,[23] such as the squared distance from the center of mass which is large in the tethering phase, and vesicle asphericity for the fluctuating and bola/prolate phases. However, for the performed simulations, a more quantitative characterization seems to be of little benefit. Possibly, the quantitative characterization might become useful for a much higher sampling density of simulated parameter space.

3.2 Membrane tension

The mean vesicle tension $\bar{\lambda}$ computed from local membrane stresses (see Appendix B) for different adhesion energies is
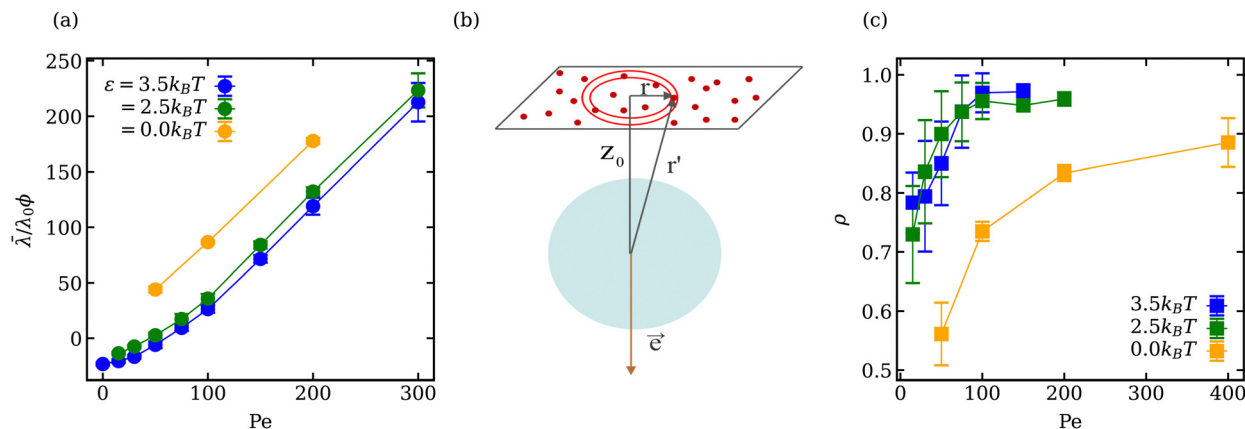
Fig. 4 (a) Mean local vesicle tension $\bar{\lambda}$ as a function of Pe for different adhesion strengths ε at $\phi = 0.18$. (b) Sketch of an ABP (blue) interacting with a flat membrane at a distance z_0. Membrane vertices are depicted in red and the orientation vector $\vec{e}$ of the ABP is pointing away from the membrane. (c) Mean fraction ρ of the ABPs in a direct contact with the membrane as a function of Pe for different ε values at $\phi = 0.18$. The error bars in (a and c) correspond to the variance of the calculated values over different time frames.

shown in Fig. 4(a). Tension is calculated every $\Delta t = 0.01\tau_r$ ($\tau_r \approx 0.1\tau$) within the time range $0.4\tau_r < t < 5\tau_r$ and averaged over all time frames. For small Pe $\lesssim 50$ in the case of adhesive ABPs, the mean tension of the vesicle is slightly negative, which indicates local compression of the membrane vertices. The local contraction of the membrane is facilitated by adhesive interactions, which are relatively long ranged, and favor the adhesion of more membrane vertices to the ABPs, leading to local compression of the membrane within the adhesion area. Furthermore, at small Pe, active particles generate a relatively low swim pressure at the membrane, so that the membrane tension remains slightly negative.

Membrane tension $\bar{\lambda}$ for $\varepsilon > 0$ in Fig. 4(a) exhibits two different regimes. For Pe < 100, the dependence of $\bar{\lambda}$ is non-linear, while for Pe > 100, $\bar{\lambda}$ increases linearly with increasing Pe, similar to the case of $\varepsilon = 0$. For active vesicles with non-adhesive ABPs, the linear growth in $\bar{\lambda}$ is determined by the swim pressure[37] of ABPs on the membrane, such that $\bar{\lambda}/\lambda_0 = \chi \mathrm{Pe}\phi$, where $\lambda_0 = R^2 k_B T/(\pi\sigma^4)$ is a normalization factor and χ is the active tension weight related to the alignment of propulsion direction with the membrane normal.[23] Therefore, the linear regime of $\bar{\lambda}$ for active vesicles with adhesive ABPs is also due to the swim pressure of ABPs on the membrane, because for large Pe, the ABP propulsion force dominates over adhesion interactions. However, the non-linear dependence of $\bar{\lambda}$ for Pe < 100 and $\varepsilon > 0$ is due to the interplay of swim pressure and particle adhesion to the membrane. Interestingly, the proportionality $\bar{\lambda} \sim \mathrm{Pe}\phi\lambda_0$ suggests that the active tension should increase as R^2 with increasing vesicle size for a fixed ABP volume fraction. This would favor prolate and bola states over tethering for large vesicles.

The location of the transition from the non-linear to the linear increase in $\bar{\lambda}$ with increasing Pe can be estimated using a simple model, where an adhesive particle placed at a distance z_0 from a flat membrane attempts to escape the surface, see Fig. 4(b). The attractive force exerted on the particle due to the membrane patch at a distance $r' = \sqrt{r^2 + z_0^2}$ with an area $2\pi r \mathrm{d}r$

is given by

$$\mathrm{d}F = 24\varepsilon \left[2\left(\frac{\sigma}{2r'}\right)^{12} - \left(\frac{\sigma}{2r'}\right)^6 \right] n \frac{z_0}{r'} \frac{2\pi r}{r'} \mathrm{d}r, \quad (9)$$

where $n = N_v/4\pi R^2$ is the number density of vertices at the membrane, and the factor z_0/r' is due to the projection of the force onto the normal-to-the-surface direction. When the propulsion direction $\vec{e}$ of the particle points away from the membrane along the normal, force balance implies

$$\mathrm{Pe} = \frac{\sigma}{k_B T}\int_0^{\sqrt{(r_c^{\mathrm{p-m}})^2 - z_0^2}} \mathrm{d}F = \frac{8\pi\varepsilon n\sigma z_0}{k_B T}\left[\left(\frac{2r'}{\sigma}\right)^{-12} - \left(\frac{2r'}{\sigma}\right)^{-6} \right]_{z_0}^{r_c^{\mathrm{p-m}}}. \quad (10)$$

This expression allows the calculation of a maximum Pe required for ABP detachment from the membrane, yielding $\mathrm{Pe}_{\max} \approx 385$ for $\varepsilon = 3.0k_B T$ and $z_0 \simeq 1.14\sigma/2$ (i.e., z_0 is the distance from the flat membrane at which the maximum in Pe is obtained). Here, the local curvature of the membrane is neglected, which would result in an increase of the detachment force. From simulations with a frozen membrane, the detachment of an ABP with $\varepsilon = 3.0k_B T$ takes place at $\mathrm{Pe}_{\max} \approx 390$, in good agreement with the analytical estimate. However, for a deformable membrane, thermal undulations lead to a steric repulsion of the ABP from the membrane,[62] which causes a decrease in the detachment force. The repulsive force exerted on the ABP by the fluctuating membrane can be estimated in terms of Pe as[63,64]

$$\mathrm{Pe}_{\mathrm{noise}} = \frac{\sigma}{k_B T}(2\pi R_{\mathrm{eff}})\frac{c(k_B T)^2}{\kappa h^2}, \quad (11)$$

where $R_{\mathrm{eff}} = 2^{1/6}\sigma/2$ is the effective radius of the particle (here, the equilibrium distance between the particle and membrane vertices), $h = z_0 - R_{\mathrm{eff}} \simeq 0.02\sigma/2$ is the distance between the ABP surface and the membrane, and c is a constant in the range $(0.01, 0.23)$.[62,64–66] Note that the magnitude of h in our case is similar to the average fluctuation amplitude $\bar{h}_\sigma$ of a flat

tensionless membrane on a length scale of the particle size σ, where $\bar{h}_\sigma = \sqrt{2k_BT/\kappa/(2\pi)^3}\sigma/2 \simeq 0.02\sigma/2$. The range of $c \in$ (0.01,0.23) corresponds to a broad range of $Pe_{noise} \in$ (20,500). Recent experiments of particle wrapping by a lipid membrane[64] suggest a much narrower range of $c \in$ (0.03,0.06), corresponding to $Pe_{noise} \in$ (65,130). Taking the median value of $Pe_{noise} \simeq 100$ for $c = 0.045$, Pe required for the ABP detachment becomes $Pe_{detach} = Pe_{max} - Pe_{noise} \simeq 290$. From simulations of a single ABP adhered to a fluctuating membrane with $\varepsilon = 3.0k_BT$, the detachment force corresponds to $Pe \simeq 200$. This Pe value is in a reasonable agreement with the theoretical estimate of Pe_{detach}, taking into account that Pe_{noise} is very sensitive to the choice of h and c. The transition from the non-linear to linear increase in $\bar{\lambda}$ in Fig. 4(a) corresponds to $Pe \approx 100$. This value is lower than the theoretical estimate, which is likely due to the presence of frequent inter-ABP collisions at $\phi = 0.18$, and enhanced membrane fluctuations facilitated by active particles (see Section 3.3). Interestingly, a shift between the $\bar{\lambda}$ curves for $\varepsilon = 0$ and $\varepsilon > 0$ in Fig. 4(a) also corresponds to about $Pe \simeq 100$.

Since membrane tension is affected by the ABP adhesion, we also compute the fraction ρ of particles which are in a direct contact with the membrane, i.e. within a distance of 0.625σ from the membrane accounting for only one layer of ABPs. ρ is measured every $\Delta t = 0.1\tau_r$ within the time range $0.4\tau_r < t < 5\tau_r$, and averaged over all time frames. Fig. 4(c) shows that ρ for adhesive ABPs is nearly twice larger than for non-adhesive particles at low Pe. As Pe is increased, ρ rapidly approaches unity for the cases with $\varepsilon > 0$ and levels off for $Pe > 100$, while in the absence of adhesion, ρ reaches a value of 0.88 only at $Pe = 400$. Therefore, adhesive interactions make a difference even at large Pe. Although the fraction ρ of near-membrane ABPs seem to follow the same trend for $\varepsilon = 0$ and $\varepsilon > 0$, the physical mechanisms are different. For $\varepsilon = 0$, an increase in Pe leads to an increase in the number of ABPs at the membrane due to activity-induced accumulation of ABPs at surfaces.[34,67] ABPs spend on average more time at the surface with increasing Pe, since the escape times decrease with decreasing rotational diffusion, leading to an increase in ρ. Furthermore, there exists a feedback mechanism between particle accumulation and membrane curvature,[18,23] as the propulsion force exerted on the membrane induces a larger local curvature and ABPs accumulate in regions of the large curvature.[35,36] For the cases with $\varepsilon > 0$, this mechanism is also partially relevant, however, already at low Pe, most of the particles are located at the membrane due to adhesive interactions. The fraction ρ at low Pe for adhesive ABPs in Fig. 4(c) does not reach unity because of the strong wrapping of particles by the membrane, whose area is insufficient for all ABPs at $\phi = 0.18$. As Pe is increased and ABPs have a sufficient force to detach from the membrane, near-equilibrium frozen "cauliflower" structures with strong particle wrapping dissolve and the activity-induced accumulation of ABPs results in ρ to approach unity. Note that even though the fraction of ABPs at the membrane for $\varepsilon > 0$ is larger than that for $\varepsilon = 0$, it does not contribute in the same way to

membrane tension. For $\varepsilon = 0$, the larger is the fraction ρ, the larger is the mean membrane tension $\bar{\lambda}$ due to an increasing swim pressure. For $\varepsilon > 0$, even though an increase in Pe leads to an increase in $\bar{\lambda}$ for the same reason, ABP adhesion reduces mean membrane tension because of long-ranged adhesive interactions discussed above. Moreover, at low Pe, a number of adhered ABPs may temporarily be oriented away from the membrane without detaching from it, which results in a reduction of the total swim pressure. Fig. 5 shows the distribution of the projection $\mathbf{e}\cdot\hat{\mathbf{r}}$ of the orientation vector $\mathbf{e}$ of ABPs onto their normalized radial position vector $\hat{\mathbf{r}}$ measured from the center of mass of the vesicle. Positive/negative values of $\mathbf{e}\cdot\hat{\mathbf{r}}$ correspond to ABP orientations toward/away from the membrane (i.e. extensile/contractile stresses). Note that at low Pe, there is a considerable fraction of ABPs in the first layer with $\mathbf{e}\cdot\hat{\mathbf{r}} < 0$, i.e. pointing away from the membrane, whereas in the second layer, the vast majority of APBs points toward the membrane. When ABPs arrive at the membrane from the bulk, they must point toward the membrane and exert extensile active stresses. At low Pe, and sufficiently strong adhesion, such that the residence time at the membrane exceeds the rotational diffusion time τ_r, ABPs in the first layer can re-orient and exert forces away from the membrane, even though they do not seem to destabilize the static shapes. At larger Pe, before the re-orientation due to rotational diffusion can take place, ABPs slide along the membrane and continue to exert extensile stresses on the membrane, which is similar to the case of $\varepsilon = 0$.[36] Furthermore, only ABPs that are in direct contact with the membrane can exert contractile stresses due to adhesion. In contrast, extensile stresses can come from all ABPs, independently of their contact with the membrane. As a result, the generated active tension is generally positive and increasing with Pe, as shown in Fig. 4(a).
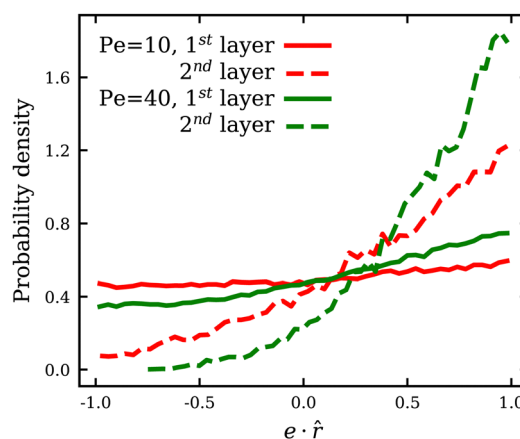

Fig. 5 Probability distribution of the projection $\mathbf{e}\cdot\hat{\mathbf{r}}$ of the orientation vector $\mathbf{e}$ of ABPs onto their normalized radial position vector $\hat{\mathbf{r}}$ measured from the center of mass of the vesicle. Positve/negative values of $\mathbf{e}\cdot\hat{\mathbf{r}}$ correspond to ABP orientations toward/away from the membrane. Solid/dashed lines mark the distributions of ABPs that are in the first/second particle layer from the membrane. Data are collected every $\Delta t = 0.01\tau_r$ within the time range $\tau_r < t < 5\tau_r$.

3.3 Vesicle shape fluctuations

In the fluctuating regime, we analyse vesicle shape changes by computing the fluctuation spectrum of a membrane cross-section, as outlined in Appendix C. Fluctuation spectra of active vesicles at $\phi = 0.18$ are presented in Fig. 6 for various ε and Pe values. The fluctuation spectra can be divided into the three regimes with respect to the mode number l: (i) low $l \lesssim 10$ where the ABP activity or adhesion dominate, (ii) intermediate $10 \lesssim l \lesssim l_\sigma$ where the competition between the ABP propulsion and adhesion is important, with $l_\sigma = 2\pi R/\sigma \simeq 50$ being a wavelength of the ABP size, and (iii) large $l \gtrsim l_\sigma$ where passive bending rigidity of the membrane dominates. At low mode numbers $l \lesssim 10$ and small Pe $\lesssim 50$ values, a plateau-like region is observed, which is more pronounced for large adhesion strengths. This indicates that large-wavelength fluctuations are suppressed in the presence of adhesion at low Pe due to nearly non-dynamic ABP clusters adhered to the membrane. The suppression of large wavelength fluctuations has also been observed in cells due to the presence of an underlying cytoskeleton.[68,69] Thus, the adhesion of particles to the membrane leads to a membrane confinement effect, significantly reducing fluctuations at low l modes. As Pe is increased, the ABPs attain sufficient propulsion force to detach from the membrane, accompanied by the disappearance of the plateau region at low l. Furthermore, the exponent β of fluctuation modes at low $l \in [2,8]$ becomes $\beta < -1$ (see the inset in Fig. 6(a)), which is a clear signature of active membrane fluctuations.[18,19] β decreases as a function of Pe, demonstrating the enhancement of low-mode fluctuations due to ABP activity.

A shift in the fluctuation-spectrum curves for different adhesion strengths and intermediate l values at Pe = 50 in Fig. 6(b) is likely due to the fact that a number of adhered ABPs can enhance membrane fluctuations by exerting temporary forces in the direction away from the membrane without detaching from it. Note that a reduction in tension for $\varepsilon > 0$ cannot significantly contribute to this shift in fluctuation spectrum, because the effect of membrane tension is expected to be present for $l \lesssim 10$–15,[18] while the observed shift extends significantly beyond those l values. Furthermore, for Pe = 200 and $\varepsilon = 2.5k_BT$ in Fig. 6(b), the shift in fluctuation spectrum nearly disappears despite the fact that the mean membrane tension is significantly larger than in the case of Pe = 50 and $\varepsilon = 0$ (see Fig. 4(a)). This suggests that the combination of ABP activity (*i.e.*, applied forces in the direction away from the membrane) and adhesion is responsible for the shift in fluctuation spectrum for Pe $\lesssim 100$.

Another interesting feature in the fluctuation spectra in Fig. 6 for adhesive ABPs with $\varepsilon > 0$ is the enhancement of amplitudes a_l^2 at $l \simeq 40$–60 corresponding to the ABP size, since $l_\sigma = 2\pi R/\sigma \simeq 50$. This local enhancement in a_l^2 represents the wrapping of adhesive ABPs by the membrane, as it is consistently reduced at Pe = 200 in comparison to Pe = 50. Finally, at large l, the squared fluctuation amplitudes decay as l^{-3} irrespective of ABP adhesion or Pe, corresponding to the bending-dominated regime of membrane fluctuations.

3.4 ABP clustering and mobility

Adhesion of ABPs to the membrane must decrease their overall mobility. Fig. 7(a) presents distributions of fixed-time displacements δ of single ABPs for various Pe and ε values in the tethering regime. The displacements are calculated for a fixed time interval $\Delta t = 0.1\tau_r$ (*i.e.* in the active-ballistic regime) within the time range $0.4\tau_r < t < 5\tau_r$. As expected, ABP mobility is significantly reduced for the cases of $\varepsilon > 0$ in comparison to non-adhesive ABPs, and the reduction in particle mobility is more pronounced at low Pe, since adhesion interactions
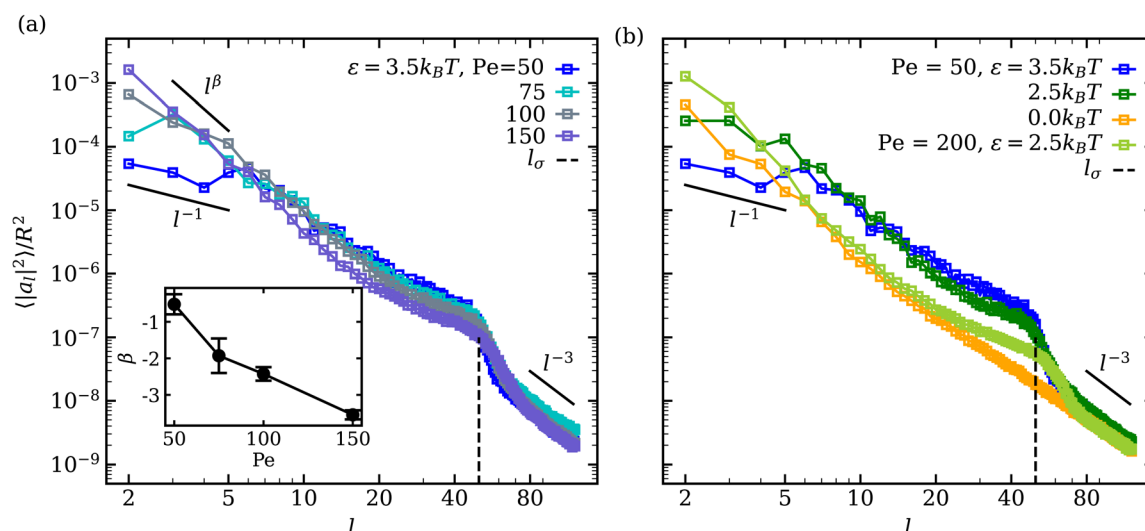

Fig. 6 Mode spectra of vesicle-shape fluctuations for $\phi = 0.18$ at (a) $\varepsilon = 3.5k_BT$ for different Pe values and at (b) Pe = 50 for different ε values. Large wavelength (low mode) fluctuations are suppressed at low Pe for a strong ABP adhesion, resulting in a plateau-like region at $l \lesssim 10$. The inset in (a) shows the exponent β of low-mode fluctuations with increasing Pe. The error bars are estimated from the covariance matrix of the fitted model.[61] The dashed lines indicate the mode number $l_\sigma = 2\pi R/\sigma \simeq 50$, representing a wavelength of the ABP size.
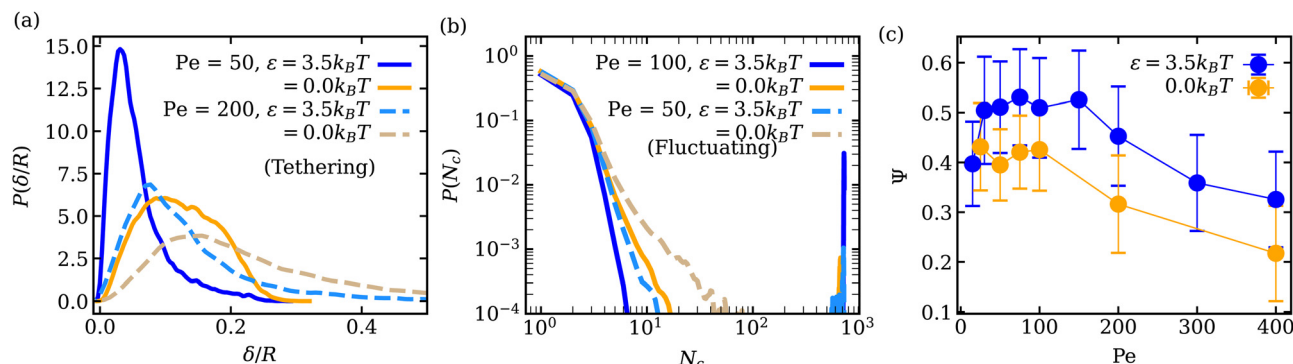
Fig. 7 (a) Distributions of fixed-time displacements δ of single ABPs for different ε and Pe values in the tethering regime for $\Delta t = 0.1\tau_r$ ($\tau_r \approx 0.1\tau$). (b) Distributions of cluster sizes N_c in the fluctuating regime at $\phi = 0.18$ for different Pe and ε. (c) Mean cluster asphericity Ψ as a function of Pe for $\varepsilon = 0$ and $\varepsilon = 3.5k_BT$. The error bars correspond to the variance of the data collected over different time frames.
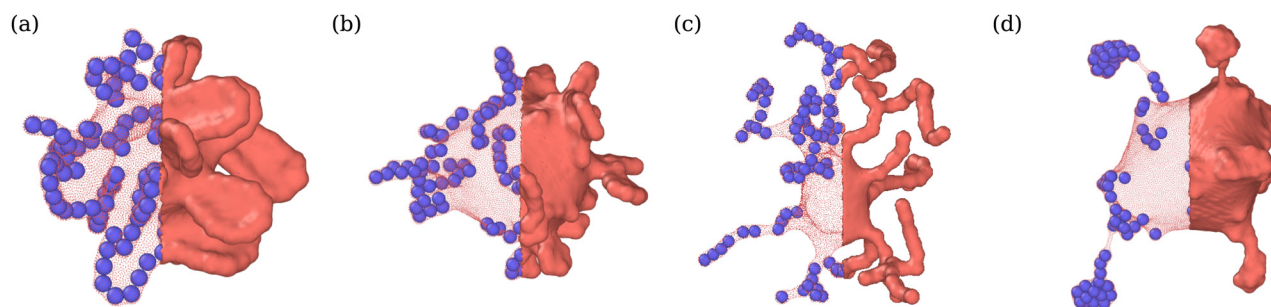

Fig. 8 Vesicle shapes for $\phi = 0.04$ and $\varepsilon = 3.5k_BT$ at (a) Pe = 15 (see Movie S4, ESI†), (b) Pe = 50, (c) Pe = 150 (see Movie S1, ESI†), and (d) Pe = 300. Particle structures change from membrane-wrapped ring-like arrangements to membrane-wrapped (branched) tubular aggregates, as Pe is increased. A further increase in Pe leads to the detachment of ABPs from the membrane and their accumulation at the tether end. The left half of the membrane is made transparent so that the arrangement of ABPs is visible.

dominate over the ABP activity. The mobility of active particles can also be reduced due to the formation of ABP clusters inside the vesicle. Fig. 7(b) shows distributions of cluster sizes N_c (*i.e.*, the number of ABPs per single cluster) at large ϕ for various Pe and ε in the fluctuating regime. The clustering analysis is performed every $\Delta t = 0.01\tau_r$ within the time range $0.4\tau_r < t < 5\tau_r$, where particles within a distance of 1.1σ are considered a part of the same cluster. In the absence of adhesion ($\varepsilon = 0$), an increase in Pe leads to an increased accumulation of ABPs at the membrane, such that large clusters are formed through a reduction in the number of small clusters, as can be seen through the emergence of a peak at large N_c for Pe = 100 in Fig. 7(b). For $\varepsilon > 0$, ABP adhesion to the membrane further facilitates the membrane-mediated formation of large particle clusters, as in this case, a peak at large N_c develops already at Pe = 50 in Fig. 7(b). As a result, adhesive interactions generally enhance cluster formation in comparison to the case of non-adhesive ABPs. Despite the strong tendency for cluster formation at the membrane surface, there are no long-range ABP velocity correlations beyond the size of clusters.

We also compute cluster asphericity Ψ (see Appendix D for details) to quantify the effect of ABP adhesion on cluster shapes. Fig. 7(c) presents Ψ as a function of Pe, and demonstrates that adhesive interactions cause an increase in the asphericity of ABP clusters. Thus, ABP clusters for $\varepsilon > 0$ attain

shapes, which are further away from a spherical geometry, in agreement with the branched string-like arrangements of ABPs in the tethering regime discussed in Section 3.1. For $\varepsilon = 0$, ABPs primarily cluster at the end of tethers as nearly spherical aggregates. Interestingly, Ψ for the case of adhesive ABPs first increases and then decreases with increasing Pe. Characteristic vesicle shapes are illustrated in Fig. 8 for different Pe. At low Pe, ring-like ABP clusters (Fig. 8(a)) in the near-equilibrium cauliflower regime are observed and have the asphericity of about $\Psi = 0.4$. With increasing Pe, branched string-like clusters of ABPs within membrane tubes develop with $\Psi > 0.4$, see Fig. 8(c). At large Pe $\gtrsim 200$, ABP propulsion forces dominate over adhesive interactions, so that the string-like structures are destabilized and the ABPs cluster at the tether ends (Fig. 8(d)) with a reduced cluster asphericity. In conclusion, the results in Fig. 7 clearly show that adhesive interactions of ABPs with the membrane strongly alter the behavior of individual ABPs and their clusters.

4. Summary and conclusions

Vesicles enclosing active particles exhibit a variety of dynamic shape deformations, ranging from tethers to prolate and bola-like shapes. Adhesive interactions between particles and

a vesicle in equilibrium can lead to strong, although static, deformations of the vesicle, such as the formation of buds and long tubular structures. In this work, we have combined the effects of particle activity and adhesion to study the deformation and properties of vesicles enclosing adhesive ABPs. At low propulsion forces of ABPs, adhesion interactions with the membrane dominate, leading to the formation of membrane structures (*e.g.*, buds, tubes) which are similar to those in equilibrium. Furthermore, due to the absence of a volume constraint in our simulations, strong membrane deformations with ring-like and sheet-like ABP structures occur for moderate volume fractions of ABPs, which are governed by the balance of adhesive interactions and energetic costs for membrane bending. As the propulsion of ABPs (or the Peclet number Pe) is increased, the particles are able to detach from the membrane, and the effects of adhesion become less dominant. A simple estimation for the detachment force of a single ABP adhered to the membrane based on theoretical arguments and simulations yields the adhesion-dominated regime for Pe $\lesssim$ 200 (depending on membrane bending rigidity, adhesion strength, and particle size). However, ABP-ABP collisions at large enough ϕ and enhanced membrane fluctuations due to the particle activity further lower the characteristic Pe $\lesssim$ 100 determining the adhesion-dominated regime. In the tethering regime, adhesion interactions between the membrane and ABPs significantly reduce the characteristic Pe for tether formation in comparison to non-adhesive ABPs. Furthermore, ABP adhesion favours the formation of long branched tether structures partially or fully filled with active particles for low to moderate volume fractions.

At large ϕ, an increase in Pe first causes 'melting' of nearly frozen particle structures within the vesicle at low Pe, such that the vesicle attains a spherical shape with pronounced membrane fluctuations. A further increase in Pe results in elongated vesicle shapes or bola-like shapes which eventually split into two daughter vesicles. Different from active vesicles with non-adhesive ABPs, for which the fluctuating regime is observed at low Pe across all ϕ values, membrane fluctuations in the presence of ABP adhesion take place only at $\phi \gtrsim 0.07$ and require some activation energy through a non-zero Pe. The fluctuation spectrum at low Pe has a plateau at low mode numbers because of a 'caging' effect due to the adhered particles. ABP adhesion to the membrane leads to local membrane compression with a slightly negative tension due to long-ranged adhesive interactions, so that the mean vesicle tension is lower in the case of adhesive ABPs than for non-adhesive particles. With increasing Pe, the mean membrane tension of the vesicle first has a non-linear dependence on Pe in the adhesion dominated regime, followed by a linear increase of the mean tension at large enough Pe $\gtrsim$ 100, in agreement with theoretical predictions from the Young-Laplace equation in the case of non-adhesive ABPs.[18,23] Furthermore, the adhesion of ABPs to the membrane leads to a reduced particle mobility, but enhances ABP clustering through membrane-mediated interactions. Also, ABP clusters in the presence of adhesive interactions have larger cluster asphericities than those for non-adhesive ABPs, mainly due to the formation of branched

string-like structures of ABPs within membrane tubes in the tethering regime. In conclusion, the presence of adhesive interactions between ABPs and the membrane affects not only the phase diagram of active vesicles, but also membrane characteristics (*e.g.*, shape, tension) and ABP properties (*e.g.*, mobility, clustering).

It is also important to mention several limitations of our study. We have focused on membranes with low bending rigidity, where the wrapping of particles is most pronounced. An increased membrane bending rigidity would reduce the degree of particle wrapping, and increase the adhesion strength required for strong wrapping.[39,40] Furthermore, the onset of tether formation for stiffer membranes should be shifted toward larger Pe numbers.[18] However, we expect that the qualitative behavior of active vesicles should remain similar. Considering membrane fluidity, a change in membrane viscosity would modify the dynamics of active vesicle structures. More importantly, hydrodynamic interactions (not taken into account in this study) are expected to affect the dynamics of active particles and the vesicle. If the membrane would possess a non-zero shear elasticity, the tethering regime will be partially or fully suppressed. These aspects of the behavior of active vesicles require further investigation.

Active vesicles can be considered as a biomimetic model of an "artificial cell" capable of non-equilibrium shape deformations, and can potentially act as biomimetic micro-robots. Here, there exists a variety of applications ranging from bioengineered cell mimics to targeted drug-delivery systems.[9,11,12] Clearly, particle adhesion serves as an additional parameter for the control and tuning of the behavior of active vesicles. An important consideration for future work is the role of hydrodynamic interactions on shape-changes, particle mobility, and the possible motility of these active systems. For example, cell motility is closely associated with dynamic morphological changes of the cell.[70,71] Moreover, rupture and splitting of active vesicles need to be studied in the future to properly capture the behavior of active vesicles at large particle loading. Such studies will open the door for the design of specific functionalities and possible applications.

Author contributions

G. G. and D. A. F. conceived the research project. P. I. performed the simulations and analysed the obtained data. All authors participated in the discussions and writing of the manuscript.

Conflicts of interest

There are no conflicts to declare.

Appendices

Appendix A: distance between membrane particles and an adhered ABP

The wrapped area A_{wrap} of an adhered ABP is computed as the number of membrane vertices within a cutoff distance r_{adh}
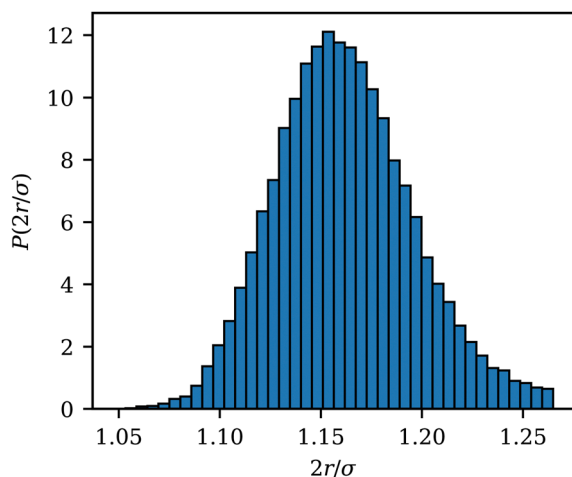
Fig. 9 Distribution function $P(2r/\sigma)$ of the scaled distance $2r/\sigma$ between an adhered ABP and membrane vertices for a fully wrapped state at Pe = 0 and $\varepsilon = 8k_{\mathrm{B}}T$.

from the ABP, multiplied by the vertex area $A_{\mathrm{v}} = A_0/N_{\mathrm{v}}$. To estimate r_{adh}, Fig. 9 shows the distribution $P(2r/\sigma)$ of the scaled distance $2r/\sigma$ between an adhered ABP and membrane vertices for a fully wrapped state at Pe = 0 and $\varepsilon = 8k_{\mathrm{B}}T$. The cutoff distance $r_{\mathrm{adh}} = 1.16\sigma/2$ for the calculation of A_{wrap} is defined as the mean of $P(2r/\sigma)$. r_{adh} is slightly larger than the minimum of the LJ potential at $r = 2^{1/6}\sigma/2$ due to contributions from the other potentials representing membrane bending resistance and local area conservation. The variance of the distribution in Fig. 9 is $\mu \simeq 0.035\sigma/2$.

Appendix B: calculation of membrane tension

Membrane tension is calculated using the virial theorem.[72] The sum over virial contributions from the local area constraint is given by

$$V_{\mathrm{av}} = \sum_{\alpha} \left\langle f_i^{\mathrm{a},\alpha} r_i^{\alpha} + f_j^{\mathrm{a},\alpha} r_j^{\alpha} + f_k^{\mathrm{a},\alpha} r_k^{\alpha} \right\rangle, \tag{12}$$

where $f_{i,j,k}^{\mathrm{a}}$ are forces at the vertices i, j and k of a triangle within the membrane triangulation, and $\alpha = x, y,$ or z represents the three coordinates. For elastic bond forces f^{b}, the virial contribution V_{b} is

$$V_{\mathrm{b}} = \sum_{\alpha} \left\langle f_i^{\mathrm{b},\alpha} r_i^{\alpha} + f_j^{\mathrm{b},\alpha} r_j^{\alpha} \right\rangle. \tag{13}$$

The total virial contribution from the forces at each vertex is then $V = V_{\mathrm{av}}/3 + V_{\mathrm{b}}/2$. The tension of the membrane is calculated as a spatial and temporal average of the local stresses as

$$\lambda = \left\langle \frac{1}{2a_i}(V_i(t) + 2k_{\mathrm{B}}T) \right\rangle_{i,t}, \tag{14}$$

where the factor two is due to the dimensionality of the membrane, $V_i(t)$ is the virial contribution at vertex i at time t, and a_i is the area of the dual cell, which is approximated by considering that each neighbouring triangle to the vertex contributes roughly one third to the area. The contribution from momentum transfer $(2k_{\mathrm{B}}T)$ is approximated by using the

equipartition theorem. The contributions from the bending energy, volume conservation, and global area conservation are not considered for membrane tension, because the bending forces mainly act perpendicular to the tension plane, while the global area and volume constraints have not been used in the simulations.

Appendix C: membrane shape fluctuations

The membrane shape fluctuations are measured by considering 2D sections of the vesicle contour in the x, y, and z directions. The sections are made every $\Delta t = 0.01\tau_{\mathrm{r}}$ within the time range of $0.4\tau_{\mathrm{r}} < t < 5\tau_{\mathrm{r}}$. The local membrane position in these contours is given by $r(\theta_m)$, where $\theta_m = 2\pi m/n$ and $2\pi/n$ is the angle for contour discretisation. The fluctuation mode amplitudes a_l are given by the decomposition[73–75]

$$a_l = \frac{1}{n} \sum_{m=0}^{n-1} r(\theta_m) \exp\left[\frac{-2\pi i l m}{n}\right]. \tag{15}$$

The complex modes a_l are calculated using the open-source FFTW[76] library, and are averaged over different time frames.

Appendix D: asphericity of ABP clusters

Shapes of ABP clusters are quantified by their asphericity. The asphericity is calculated from the gyration tensor G, which is based on the second moments of N particle positions as

$$G_{xy} \equiv \frac{1}{N} \sum_{i=1}^{N} r_x^i r_y^i, \tag{16}$$

where r is measured from the center of mass of the N-particle system, $i.e.$ $\sum_{i=1}^{N} \mathbf{r}_i = 0$. Let λ_1, λ_2, and λ_3 be the eigenvalues of G. Then, the asphericty Ψ is defined as[77]

$$\Psi = \frac{(\lambda_1 - \lambda_2)^2 + (\lambda_2 - \lambda_3)^2 + (\lambda_1 - \lambda_3)^2}{2(\lambda_1 + \lambda_2 + \lambda_3)^2}. \tag{17}$$

Values of Ψ range between 0 and 1, with $\Psi = 0$ for a perfectly spherical shape, $\Psi = 1$ for a long thin rod, and $\Psi = 0.25$ for a thin plate.

Appendix E: description of movies

All movies are for an adhesion strength of $\varepsilon = 3.5k_{\mathrm{B}}T$.

Movie S1 (ESI†): Formation of dynamic and highly branched tether structures at Pe = 150 and $\phi = 0.04$. As ABP motion along the tether is limited due to their string-like arrangement, rotational diffusion of the ABPs facilitates tether branching in contrast to ABP escape from the tether for $\varepsilon = 0$.

Movie S2 (ESI†): Tether formation at Pe = 300 and $\phi = 0.009$. ABPs can escape from a tether and join new tethers due to their rotational diffusion.

Movie S3 (ESI†): Vesicle elongation followed by splitting in the bola regime at Pe = 200 and $\phi = 0.12$.

Movie S4 (ESI†): Formation of nearly static ring-like structures of ABPs at Pe = 15 and $\phi = 0.04$.

Acknowledgements

Notes and references

1 S. Ramaswamy, *Annu. Rev. Condens. Matter Phys.*, 2010, **1**, 323–345.

2 F. Jülicher, S. W. Grill and G. Salbreux, *Rep. Prog. Phys.*, 2018, **81**, 076601.

3 G. Gompper, *et al.*, *J. Phys.: Condens. Matter*, 2020, **32**, 193001.

4 S. Shankar, A. Souslov, M. J. Bowick, M. C. Marchetti and V. Vitelli, *Nat. Rev. Phys.*, 2022, **4**, 380–398.

5 M. Kelkar, P. Bohec and G. Charras, *Curr. Opin. Cell Biol.*, 2020, **66**, 69–78.

6 X. Trepat and E. Sahai, *Nat. Phys.*, 2018, **14**, 671–682.

7 J. Elgeti, R. G. Winkler and G. Gompper, *Rep. Prog. Phys.*, 2015, **78**, 056601.

8 C. Bechinger, R. Di Leonardo, H. Löwen, C. Reichhardt, G. Volpe and G. Volpe, *Rev. Mod. Phys.*, 2016, **88**, 045006.

9 D. Needleman and Z. Dogic, *Nat. Rev. Mater.*, 2017, **2**, 17048.

10 S. Banerjee, M. L. Gardel and U. S. Schwarz, *Annu. Rev. Condens. Matter Phys.*, 2020, **11**, 421–439.

11 P. Schwille, *et al.*, *Angew. Chem., Int. Ed.*, 2018, **57**, 13382–13392.

12 A. Bernheim-Groswasser, N. S. Gov, S. A. Safran and S. Tzlil, *Adv. Mater.*, 2018, **30**, 1707028.

13 F. C. Keber, E. Loiseau, T. Sanchez, S. J. DeCamp, L. Giomi, M. J. Bowick, M. C. Marchetti, Z. Dogic and A. R. Bausch, *Science*, 2014, **345**, 1135–1139.

14 G. Duclos, R. Adkins, D. Banerjee, M. S. E. Peterson, M. Varghese, I. Kolvin, A. Baskaran, R. A. Pelcovits, T. R. Powers, A. Baskaran, F. Toschi, M. F. Hagan, S. J. Streichan, V. Vitelli, D. A. Beller and Z. Dogic, *Science*, 2020, **367**, 1120–1124.

15 K. Weirich, K. L. Dasbiswas, T. A. Witten, S. Vaikuntanathan and M. L. Gardel, *Proc. Natl. Acad. Sci. U. S. A.*, 2019, **116**, 11125–11130.

16 J. Steinkühler, R. L. Knorr, Z. Zhao, T. Bhatia, S. M. Bartelt, S. Wegner, R. Dimova and R. Lipowsky, *Nat. Commun.*, 2020, **11**, 905.

17 Y. Elani, *Angew. Chem., Int. Ed.*, 2021, **60**, 5602–5611.

18 H. R. Vutukuri, M. Hoore, C. Abaurrea-Velasco, L. van Buren, A. Dutto, T. Auth, D. A. Fedosov, G. Gompper and J. Vermant, *Nature*, 2020, **586**, 52–56.

19 S. C. Takatori and A. Sahu, *Phys. Rev. Lett.*, 2020, **124**, 158102.

20 L. Le Nagard, A. T. Brown, A. Dawson, V. A. Martinez, W. C. K. Poon and M. Staykova, *Proc. Natl. Acad. Sci. U. S. A.*, 2022, **119**, e2206096119.

21 M. Park, K. Lee and S. Granick, *Soft Matter*, 2022, **18**, 6419–6425.

22 M. Paoluzzi, R. Di Leonardo, M. C. Marchetti and L. Angelani, *Sci. Rep.*, 2016, **6**, 34146.

23 P. Iyer, G. Gompper and D. A. Fedosov, *Soft Matter*, 2022, **18**, 6868–6881.

24 Y. Li and P. R. Ten Wolde, *Phys. Rev. Lett.*, 2019, **123**, 148003.

25 M. S. Peterson, A. Baskaran and M. F. Hagan, *Nat. Commun.*, 2021, **12**, 1–9.

26 P. K. Mattila and P. Lappalainen, *Nat. Rev. Mol. Cell Biol.*, 2008, **9**, 446–454.

27 M. Krause and A. Gautreau, *Nat. Rev. Mol. Cell Biol.*, 2014, **15**, 577–590.

28 S. Tuvia, A. Almagor, A. Bitler, S. Levin, R. Korenstein and S. Yedgar, *Proc. Natl. Acad. Sci. U. S. A.*, 1997, **94**, 5045–5049.

29 Y.-K. Park, C. A. Best, T. Auth, N. S. Gov, S. A. Safran, G. Popescu, S. Suresh and M. S. Feld, *Proc. Natl. Acad. Sci. U. S. A.*, 2010, **107**, 1289–1294.

30 H. Turlier, D. A. Fedosov, B. A. Audoly, T. Auth, N. S. Gov, C. Sykes, J.-F. Joanny, G. Gompper and T. Betz, *Nat. Phys.*, 2016, **12**, 513–519.

31 U. Seifert, K. Berndl and R. Lipowsky, *Phys. Rev. A*, 1991, **44**, 1182–1202.

32 R. Lipowsky, *Faraday Discuss.*, 2013, **161**, 305–331.

33 R. Lipowsky, *Adv. Colloid Interface Sci.*, 2022, **301**, 102613.

34 Y. Fily, A. Baskaran and M. F. Hagan, *Soft Matter*, 2014, **10**, 5609–5617.

35 Y. Fily, A. Baskaran and M. F. Hagan, *Phys. Rev. E: Stat., Nonlinear, Soft Matter Phys.*, 2015, **91**, 012125.

36 P. Iyer, R. G. Winkler, D. A. Fedosov and G. Gompper, *arXiv*, 2022, preprint, arXiv:2212.08561, DOI: **10.48550/arXiv.2212.08561**.

37 S. C. Takatori, W. Yan and J. F. Brady, *Phys. Rev. Lett.*, 2014, **113**, 028103.

38 R. Lipowsky and H.-G. Döbereiner, *EPL*, 1998, **43**, 219.

39 M. Deserno and T. Bickel, *EPL*, 2003, **62**, 767.

40 S. Dasgupta, T. Auth and G. Gompper, *Nano Lett.*, 2014, **14**, 687–693.

41 M. Raatz, R. Lipowsky and T. R. Weikl, *Soft Matter*, 2014, **10**, 3570–3577.

42 S. Dasgupta, T. Auth and G. Gompper, *J. Phys.: Condens. Matter*, 2017, **29**, 373003.

43 I. Koltover, J. O. Raedler and C. R. Safinya, *Phys. Rev. Lett.*, 1999, **82**, 1991.

44 A. Šarić and A. Cacciuto, *Phys. Rev. Lett.*, 2012, **109**, 188101.

45 A. Šarić and A. Cacciuto, *Phys. Rev. Lett.*, 2012, **108**, 118101.

46 J. Cardellini, L. Caselli, E. Lavagna, S. Salassi, H. Amenitsch, M. Calamai, C. Montis, G. Rossi and D. Berti, *J. Phys. Chem. C*, 2022, **126**, 4483–4494.

47 A. H. Bahrami and T. R. Weikl, *Nano Lett.*, 2018, **18**, 1259–1263.

48 I. Canton and G. Battaglia, *Chem. Soc. Rev.*, 2012, **41**, 2718–2739.

49 S. Tzlil, M. Deserno, W. M. Gelbart and A. Ben-Shaul, *Biophys. J.*, 2004, **86**, 2037–2048.

50 A. Aderem and D. M. Underhill, *Annu. Rev. Immunol.*, 1999, **17**, 593–623.

51 J. S. Rossman and R. A. Lamb, *Virology*, 2011, **411**, 229–236.

52 G. Gompper and D. M. Kroll, *Statistical mechanics of membranes and surfaces*, World Scientific, Singapore, 2nd edn, 2004, pp. 359–426.

53 D. M. Kroll and G. Gompper, *Science*, 1992, **255**, 968–971.

54 H. Noguchi and G. Gompper, *Phys. Rev. E: Stat., Nonlinear, Soft Matter Phys.*, 2005, **72**, 011901.

55 W. Helfrich, *Z. Naturforschung C*, 1973, **28**, 693–703.

56 G. Gompper and D. M. Kroll, *J. Phys. I France*, 1996, **6**, 1305–1320.

57 G. Gompper and D. M. Kroll, *J. Phys.: Condens. Matter*, 1997, **9**, 8795–8834.

58 H. Noguchi and G. Gompper, *Phys. Rev. Lett.*, 2004, **93**, 258102.

59 M. P. Allen and D. J. Tildesley, *Computer simulation of liquids*, Clarendon Press, New York, 1991.

60 J. Agudo-Canalejo and R. Lipowsky, *Soft Matter*, 2016, **12**, 8155–8166.

61 P. H. Richter, TDAPR, 1995.

62 W. Helfrich, *Z. Naturforsch.*, 1978, **33**, 305–315.

63 T. Bickel, *J. Chem. Phys.*, 2003, **118**, 8960–8968.

64 H. T. Spanke, R. W. Style, C. François-Martin, M. Feofilova, M. Eisentraut, H. Kress, J. Agudo-Canalejo and E. R. Dufresne, *Phys. Rev. Lett.*, 2020, **125**, 198102.

65 A. D. Dinsmore, D. T. Wong, P. Nelson and A. G. Yodh, *Phys. Rev. Lett.*, 1998, **80**, 409–412.

66 G. Gompper and D. M. Kroll, *Europhys. Lett.*, 1989, **9**, 59–64.

67 J. Elgeti and G. Gompper, *Europhys. Lett.*, 2013, **101**, 48003.

68 N. Gov and S. Safran, *Biophys. J.*, 2005, **88**, 1859–1874.

69 N. Gov, A. Zilman and S. Safran, *Phys. Rev. Lett.*, 2003, **90**, 228101.

70 K. M. Yamada and M. Sixt, *Nat. Rev. Mol. Cell Biol.*, 2019, **20**, 738–752.

71 A. Shellard and R. Mayor, *Trends Cell Biol.*, 2020, **30**, 852–868.

72 D. Tsai, *Chem. Phys.*, 1979, **70**, 1375–1382.

73 J. Pécréaux, H.-G. Döbereiner, J. Prost, J.-F. Joanny and P. Bassereau, *Eur. Phys. J. E*, 2004, **13**, 277–290.

74 H. A. Faizi, C. J. Reeves, V. N. Georgiev, P. M. Vlahovska and R. Dimova, *Soft Matter*, 2020, **16**, 8996–9001.

75 J. Faucon, M. Mitov, P. Méléard, I. Bivas and P. Bothorel, *J. Phys.*, 1989, **50**, 2389–2414.

76 M. Frigo and S. G. Johnson, *Proc. IEEE*, 2005, **93**, 216–231.

77 J. Rudnick and G. Gaspari, *J. Phys. A: Math. Gen.*, 1986, **19**, L191–L193.

78 Jülich Supercomputing Centre, *J. Large-Scale Res. Facil.*, 2021, **7**, A182.